Received: 15 June 2021 | Revised: 8 November 2021 | Accepted: 15 November 2021

DOI: 10.1002/mrm.29110

RESEARCH ARTICLE

Magnetic Resonance in Medicine

Genetic algorithm-based optimization of pulse sequences

Vencel Somai[1,2] | **Felix Kreis**[3] | **Adam Gaunt**[1] | **Anastasia Tsyben**[1] | **Ming Li Chia**[1] | **Friederike Hesse**[1] | **Alan J. Wright**[1] | **Kevin M. Brindle**[1,4]

[1]Cancer Research UK Cambridge Institute, University of Cambridge, Cambridge, United Kingdom

[2]Department of Radiology, School of Clinical Medicine, University of Cambridge, Cambridge, United Kingdom

[3]Institute for Biomedical Engineering, University of Zurich and ETH Zurich, Zurich, Switzerland

[4]Department of Biochemistry, University of Cambridge, Cambridge, United Kingdom

Correspondence
Vencel Somai, Cancer Research UK Cambridge Institute, Li Ka Shing Centre, Robinson Way, Cambridge, CB2 0RE, UK.
Email: Vencel.Somai@cruk.cam.ac.uk

Funding information
Supported by the Cancer Research UK Cambridge Institute Biological Resources Unit and Preclinical Imaging Core Facilities. Funding provided by the European Union's Horizon 2020 Research and Innovation Program under Future and Emerging Technologies (FET) Open grant agreement 858149 (AlternativesToGd); and by Cancer Research UK, grants C197/A16465; C55296/A26605; and C9685/A25177

Purpose: The performance of pulse sequences in vivo can be limited by fast relaxation rates, magnetic field inhomogeneity, and nonuniform spin excitation. We describe here a method for pulse sequence optimization that uses a stochastic numerical solver that in principle is capable of finding a global optimum. The method provides a simple framework for incorporating any constraint and implementing arbitrarily complex cost functions. Efficient methods for simulating spin dynamics and incorporating frequency selectivity are also described.
Methods: Optimized pulse sequences for polarization transfer between protons and X-nuclei and excitation pulses that eliminate J-coupling modulation were evaluated experimentally using a surface coil on phantoms, and also the detection of hyperpolarized [2-^{13}C]lactate in vivo in the case of J-coupling modulation-free excitation.
Results: The optimized polarization transfer pulses improved the SNR by ~50% with a more than twofold reduction in the B_1 field, and J-coupling modulation-free excitation was achieved with a more than threefold reduction in pulse length.
Conclusion: This process could be used to optimize any pulse when there is a need to improve the uniformity and frequency selectivity of excitation as well as to design new pulses to steer the spin system to any desired achievable state.

KEYWORDS
hyperpolarized, metabolism, MRI, numerical optimization, pulse sequence

1 | INTRODUCTION

Pulse sequence design can be challenging due to both a complex theoretical description and hardware limitations. To address these problems, optimization-based approaches have been introduced.[1–5] However, many operate by optimizing a unitary transformation, which manipulates the spin system to the desired state, even in the presence of experimental limitations.[3,4,6] A caveat is that the operator must be known in advance and optimization is restricted to simple design scenarios.[6] For the more general case of state-to-state optimization, Khaneja et al.[1] introduced an optimal control-based technique, which has found many applications.[7–12] The limitation of this approach is that the optimization can

get trapped in local minima,[1] and the gradient of the cost function can be difficult to calculate. Another constraint is that the time-steps be constant,[1] imposing a further restriction on the process. As a potential solution for nonconvex-constrained optimization problems, a genetic algorithm was proposed,[13] which is a stochastic solver working with a population of solutions. Convergence to a global optimum is possible with no initial guess and convexity requirements on the cost function. A further advantage is that a cost-function gradient does not need to be calculated, yielding a simple framework that can incorporate any constraint and can be used to compose arbitrarily complex cost functions. Veglia et al[2] introduced a genetic algorithm-based approach for optimized spin dynamics, but this optimizes only the phases of a fixed number of pulses and delays between the pulses in order to avoid the need for spin dynamics simulations. Here we present a more general approach, which includes an efficient method for spin dynamics simulations and incorporates frequency selectivity. The optimization process was used here to design improved pulse sequences for transferring polarization from hyperpolarized X nuclei to spin coupled protons with the aim of increasing the sensitivity of detection of hyperpolarized ^{13}C and ^{15}N-labeled metabolites.[14–16] Given the reciprocity of this polarization transfer process, we used thermally polarized instead of hyperpolarized metabolites and compared the performance of the optimized pulses to the conventional insensitive nuclei enhanced by polarization transfer (INEPT) pulse sequence[17] for transferring polarization from protons to X nuclei in [1-^{13}C]lactate, [2-^{13}C]lactate, and [$^{15}N_2$]urea. The former shows weak J-coupling, for which relaxation losses are mainly responsible for decreased sensitivity. The latter 2 are examples of strong J-coupling where the validity of the product operator formalism, which assumes instantaneous rotations, is compromised; and for [2-^{13}C]lactate, the several ms long adiabatic pulses used in experiments with surface coils in vivo to improve B_1 field uniformity cannot fit into the ideal time window of the polarization transfer block. With [$^{15}N_2$] urea, we also demonstrate the feasibility of partial transfer of polarization from the hyperpolarized ^{15}N nucleus to the spin-coupled protons.[15] Finally, we design excitation pulses that result in the selection of a single component of the ^{13}C and ^{15}N multiplets in [2-^{13}C]lactate and [$^{15}N_2$]urea respectively, which eliminate J-coupling–associated image artefacts, and compare the results obtained with the solution proposed in Ref. [18].

2 | THEORY

The optimization treats the pulse sequence as a shaped pulse with arbitrary amplitude, phase, and duration at each pulse point on each frequency channel. The cost function contains the spin dynamics simulation and a subsequent Bloch simulation to yield the desired frequency selectivity.

2.1 | Encoding the solutions

The shaped pulse at each frequency (e.g., ^{13}C and ^{1}H) is discretized to N number of time-steps. During each time-step, every pulse has an amplitude (B_1), duration (τ), and phase (Φ) (Figure 1). For delays, the RF amplitude of the time-step is set to 0. The only restriction is the number of time-steps. The minimum length of the time-steps can be constrained by the time resolution of the waveform-generator and the amplitudes of the RF pulses by the performance of the RF amplifier and transmit coil. Duty cycle constraints can also be incorporated as a penalty term in the cost function. Including the length of the pulse points in the optimization variables increased the flexibility of the algorithm; however, the final pulses had to be adjusted to match the RF raster time, which was 4 μs. This entailed rounding of the time-steps to integer multiples of the raster time and a slight correction in the corresponding amplitude. This had no noticeable effect on pulse performance. Alternatively, the time-steps can be constrained during the optimization to only take values that are integer multiples of the raster time.

2.2 | Smoothness and amplitude constraints on shaped pulses

Because RF coils and amplifiers cannot produce arbitrarily high B_1 fields or produce an instantaneous change in pulse amplitude, the amplitudes of the shaped pulses were truncated to a user-defined maximum value and then projected onto a set of waveforms with prescribed upper bounds on the first and second derivatives for each iteration of the optimization. The result is a smoothed equivalent, which is the closest to the original input waveform in the function norm defined in Equation 1. This is a convex problem that can be solved efficiently with accelerated proximal gradient descent.[19]

$$\begin{aligned} RF_{amp} &= \underset{RF_{amp}\in \boldsymbol{S}}{\operatorname{argmin}} \frac{1}{2}\left\| RF_{amp} - RF_{amp,input}\right\|_2^2 \\ \text{where} \boldsymbol{S} &:= \left\{ s\in \mathbb{R}^{\boldsymbol{N}}; \|\dot{\boldsymbol{s}}\|_\infty < \alpha, \|\ddot{\boldsymbol{s}}\|_\infty < \beta \right\} \\ \text{and } \left\| RF_{amp} - RF_{amp,input}\right\|_2^2 &:= \int_0^{T_{RF}} \left\| RF_{amp}(t) - RF_{amp,input}(t)\right\|_2^2 \mathrm{d}t. \end{aligned} \tag{1}$$

This projection does not add a noticeable increase to the run time of the cost function evaluation (Figure 2) and gave smooth changes in spin dynamics with respect to B_1 deviations and frequency offsets. This allowed the use of very coarse B_1 and frequency offset grids and accelerated considerably solver

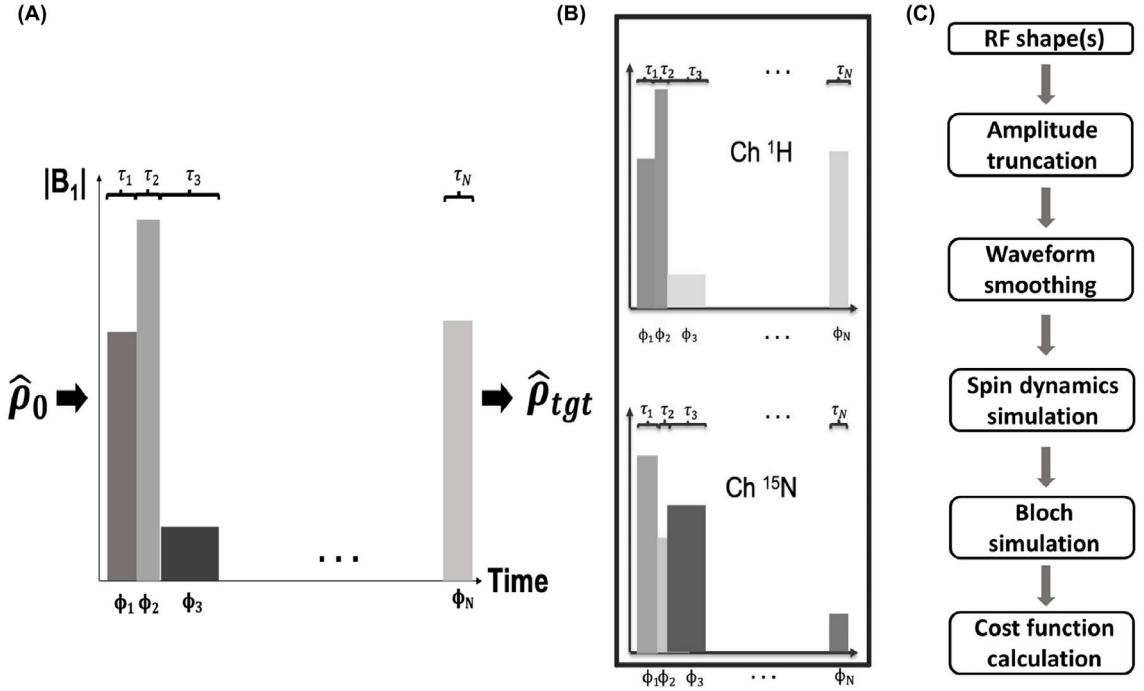

FIGURE 1 Parameters used in pulse sequence optimization (A). The parameters are the amplitude (B_1), phase (Φ_i) and the length (τ_i) of the individual pulse points. A shaped pulse is played out on the RF channel(s), which steer the initial density operator ($\hat{\rho}_0$) to the target density operator ($\hat{\rho}_{tgt}$). In a heteronuclear polarization transfer experiment, there are two RF channels: one for proton and one for the X-nucleus (B). Flowchart for calculation of the cost function (C). Φ_i, phase; τ_i, length; B_1, amplitude

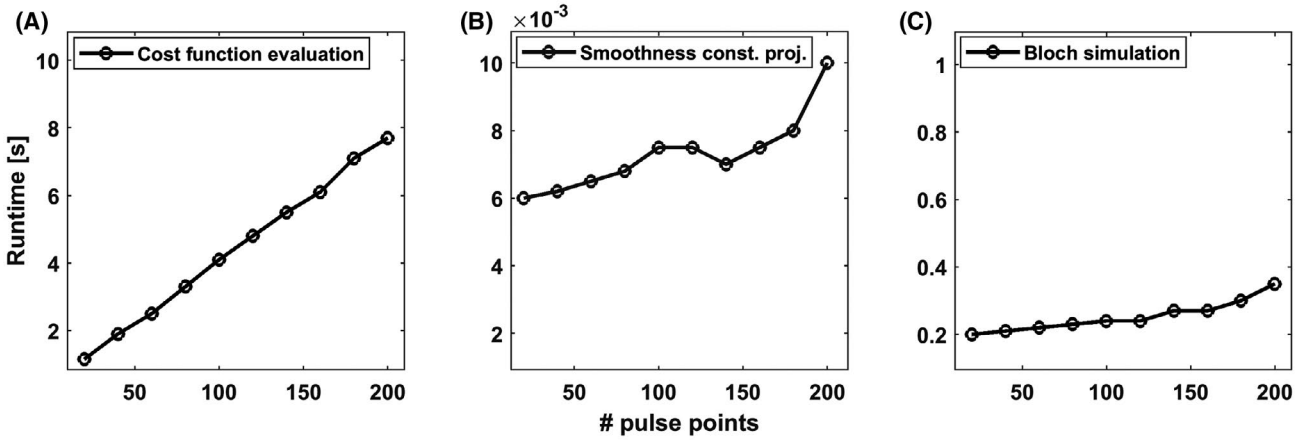

FIGURE 2 (A) Runtime of the cost function evaluation for 5 coupled spins as a function of the number of RF pulse points. The additional runtime for implementation of the smoothness constraint (B) and the Bloch simulation for enforcing frequency selectivity (C) was negligible in comparison (6–10 ms and 200–400 ms, respectively). The runtime analysis for the Bloch simulation also illustrates the speed of the proposed method for pulse sequence design when there is no spin–spin coupling

iterations. The values of α and β were selected empirically and had no noticeable effect on the runtime.

2.3 | Cost function and spin-dynamics simulations

The spin system Hamiltonian contains interaction terms for the nuclear spins with the external magnetic field and with each other. By adding RF pulses, a general effective Hamiltonian can be simulated. In Liouville-space, the equation of motion for the density operator (ρ) in the presence of relaxation can be written as[20]:

$$\dot{\hat{\rho}} = \widehat{\mathscr{L}}\hat{\rho} = \left(-i\widehat{\mathscr{H}} + \hat{\hat{\Gamma}}\right)\hat{\rho} = \left\{-i\left(\widehat{\mathscr{H}}_0 + \sum_{k=1}^{d}\widehat{\mathscr{H}}_k\right) + \hat{\hat{\Gamma}}\right\}\hat{\rho}, \quad (2)$$

where $\widehat{\widehat{\mathscr{H}}}_0$ is the free-evolution Hamiltonian superoperator; $\widehat{\widehat{\mathscr{H}}}_k$ are the RF field Hamiltonian superoperators corresponding to the different frequency channels and coordinate axes (d is the overall number of degrees of freedom, therefore for 2 RF channels $d = 4$); and $\hat{\hat{\Gamma}}$ is the thermally corrected[21,22] relaxation superoperator. With a discretized shaped pulse, when the Liouvillian of the individual pulse points is time-independent, the evolution of the density operator is given by the N propagator through the N time-steps:

$$\hat{U}_m = \exp\left\{\widehat{\mathscr{L}}_m \tau_m\right\} = \exp\left\{\left[-i\left(\widehat{\widehat{\mathscr{H}}}_0 + \sum_{k=1}^{d}\widehat{\widehat{\mathscr{H}}}_{k,m}\right) + \hat{\hat{\Gamma}}\right]\tau_m\right\}. \tag{3}$$

The density operator at the end of the pulse sequence is:

$$\hat{\rho}_{end} = \hat{\hat{U}}_N \cdots \hat{\hat{U}}_m \cdots \hat{\hat{U}}_1 \hat{\rho}_0. \tag{4}$$

The value of the cost function can be obtained by comparing the final density operator, which is the result after the propagator train, to the preferred density operator. The preferred density operator reflects the desired result, for example, that all of the available magnetization is on the proton x-axis.

The pulse sequence has to be robust to the effects of B_0 and B_1 field inhomogeneities. Therefore, the cost function is evaluated over a range of frequency offsets and B_1 amplitudes. The final fitness of the solution is the weighted average of these cost function values for which the weights account for the width of the resonance and the expected B_1 variation over this range of frequencies. These weights were assigned according to Gaussian distributions.

2.4 | Spin systems

The Hamiltonian of the [1-^{13}C]lactate spin-system in the presence of RF irradiation in the doubly rotating frame, with magnetic equivalence of the 3 methyl protons, is:

$$\begin{gathered}\hat{\boldsymbol{H}} = \hat{\boldsymbol{H}}_{free} + \hat{\boldsymbol{H}}_{RF} \\ \hat{\boldsymbol{H}}_{free} = \Delta\Omega_I \hat{\boldsymbol{I}}_{\boldsymbol{z}} + \Delta\Omega_S \hat{\boldsymbol{S}}_{\boldsymbol{z}}^{\boldsymbol{CH_3}} + \left(\Delta\Omega_S + \Omega_{S^{CH}}\right)\hat{\boldsymbol{S}}_{\boldsymbol{z}}^{\boldsymbol{CH}} + 2\pi J_{CH3}\hat{\boldsymbol{I}}_{\boldsymbol{z}}\hat{\boldsymbol{S}}_{\boldsymbol{z}}^{\boldsymbol{CH_3}} + 2\pi J_{CH}\hat{\boldsymbol{I}}_{\boldsymbol{z}}\hat{\boldsymbol{S}}_{\boldsymbol{z}}^{\boldsymbol{CH}} + 2\pi J_{HH3}\hat{\boldsymbol{S}}_{\boldsymbol{z}}^{\boldsymbol{CH}}\hat{\boldsymbol{S}}_{\boldsymbol{z}}^{\boldsymbol{CH_3}} \\ \hat{\boldsymbol{H}}_{RF} = \omega_I\left(\cos(\phi_I)\hat{\boldsymbol{I}}_{\boldsymbol{x}} + \sin(\phi_I)\hat{\boldsymbol{I}}_{\boldsymbol{y}}\right) + \omega_S\left(\cos(\phi_S)\hat{\boldsymbol{S}}_{\boldsymbol{x}} + \sin(\phi_S)\hat{\boldsymbol{S}}_{\boldsymbol{y}}\right),\end{gathered} \tag{5}$$

where $\hat{\boldsymbol{S}}_{\boldsymbol{z}}^{\boldsymbol{CH_3}} = \hat{\boldsymbol{S}}_{\boldsymbol{z}}^{\boldsymbol{CH}_{3,1}} + \hat{\boldsymbol{S}}_{\boldsymbol{z}}^{\boldsymbol{CH}_{3,2}} + \hat{\boldsymbol{S}}_{\boldsymbol{z}}^{\boldsymbol{CH}_{3,3}}$ is the sum of the individual spin operators, and $\hat{\boldsymbol{I}}_{\boldsymbol{xy}}$ and $\hat{\boldsymbol{S}}_{\boldsymbol{xy}}$ denote operators for the carbon and proton spins, respectively. The spin system in [2-^{13}C]lactate is the same as for [1-^{13}C]lactate except that the J-couplings and relaxation times differ and the methine proton is on resonance; therefore, the off-resonance term is $\Omega_{S^{CH_3}}\hat{\boldsymbol{S}}_{\boldsymbol{z}}^{\boldsymbol{CH_3}}$.

In [$^{15}N_2$]uream there are 2 pairs of protons, each pair coupled to one ^{15}N nucleus. Therefore, the Hamiltonian of the spin system in the presence of RF irradiation in the doubly rotating frame is:

$$\begin{gathered}\hat{\boldsymbol{H}} = \hat{\boldsymbol{H}}_{free} + \hat{\boldsymbol{H}}_{RF} \\ \hat{\boldsymbol{H}}_{free} = \Delta\Omega_I \hat{\boldsymbol{I}}_{\boldsymbol{z}} + \Delta\Omega_S \hat{\boldsymbol{S}}_{\boldsymbol{z}} + 2\pi J \hat{\boldsymbol{I}}_{\boldsymbol{z}}\hat{\boldsymbol{S}}_{\boldsymbol{z}} \\ \hat{\boldsymbol{H}}_{RF} = \omega_I\left(\cos(\phi_I)\hat{\boldsymbol{I}}_{\boldsymbol{x}} + \sin(\phi_I)\hat{\boldsymbol{I}}_{\boldsymbol{y}}\right) + \omega_S\left(\cos(\phi_S)\hat{\boldsymbol{S}}_{\boldsymbol{x}} + \sin(\phi_S)\hat{\boldsymbol{S}}_{\boldsymbol{y}}\right).\end{gathered} \tag{6}$$

The dual-tuned surface coils used enabled simultaneous pulsing on both frequency channels; therefore, the RF pulse terms for both protons and X-nuclei are present in $\hat{\boldsymbol{H}}_{RF}$.

2.5 | Approximation used in the spin dynamics simulations

Simulation of the spin dynamics scales exponentially with the number of spins and quickly becomes computationally intensive and often unfeasible. Numerous approaches have been introduced to tackle this problem.[23–28] These build mostly on the inherent symmetries of the spin system and reduce the matrix size by means of state space restriction methods. Simulation of the 5 spins in [1-^{13}C] lactate yields a Liouvillian matrix with dimensions of 1024×1024. Exponentiation of such a matrix is computationally expensive. Repeating it at every pulse sequence element for every member of the genetic algorithm population in every iteration makes the optimization unfeasible, even when Krylov propagation[29] is used. State space reduction methods are designed to reduce significantly the dimensionality but are more efficient for larger spin systems. Instead, the following approximation was used:

$$\boldsymbol{e}^{-\left(i\hat{\hat{\boldsymbol{H}}}+\hat{\hat{\Gamma}}\right)\tau} \approx \boldsymbol{e}^{-\frac{\hat{\hat{\Gamma}}\tau}{2}}\boldsymbol{e}^{-i\hat{\hat{\boldsymbol{H}}}\tau}\boldsymbol{e}^{-\frac{\hat{\hat{\Gamma}}\tau}{2}}. \tag{7}$$

The error of this approximation for noncommuting operators has an upper bound,[30] and the discrepancy is small provided that the *relaxation rates* $\ll$ *effective rotation field*. For the optimization process, close approximation is not required if the monotonicity of the cost function is preserved. This means that the location of the minima are preserved, and a minimizer of the transformed cost function is also a minimizer of the original cost function. Splitting of the Liouvillian is especially

useful for hyperpolarized experiments, for which the thermal correction in the relaxation superoperator becomes redundant,[14,15,31] yielding a diagonal matrix when the phenomenological relaxation model is used. Therefore, the approximate spin dynamics can be simulated in Hilbert space, which reduces the matrix size to 32×32 and, in the uncorrelated random fields relaxation regime, the exponentiation of the relaxation matrix can be performed by using a matrix composed of the exponentials of the entries. The situation is similar for thermally polarized samples with long T_1 times, for which signal recovery during the RF pulse sequence can be neglected. This approximation reduced the computational time by more than a hundredfold. This means that the relaxation superperator had diagonal entries containing only the relaxation rates. Higher-order spin terms were assumed to relax with the sum of the individual relaxation rates. For example, the time required for 1 iteration of the solver for the [1-^{13}C]lactate spin system decreased from > 500 s to ~2–5 s (Figure 2A). The polarization transfer sequences required approximately 1000 solver iterations, resulting in a total runtime of approximately 1 h. The J-coupling artefact-free excitation pulse required approximately 10 min. The convergence criterion was met when the decrease in the cost value was < 1% over the course of 50 solver iterations. If a specific problem needs higher performance, or to test optimality, the solver can be restarted; the output solution can be used as 1 member of the initializer population, which is otherwise a completely random sample. In off-line optimization-based design processes, it is often acceptable to allow several days of run time.[6,32]

2.6 | Validation of the simulations

The spin dynamics in the cost function of the optimization and the predicted transfer values were simulated with in-house MatLab (version 2020a; Mathworks, Natick, MA) scripts. The peak transfer values were confirmed using SpinDynamica (www.spindynamica.soton.ac.uk) in Wolfram Mathematica (version 11; Wolfram Research, Inc, Champaign, IL). When relaxation losses were estimated, the *PhenomenologicalRelaxationSuperoperator* function was used with the indicated T_1 and T_2 relaxation times.

2.7 | Achieving frequency selectivity

Following the spin dynamics simulation, a subsequent Bloch simulation was inserted to yield the desired frequency selectivity. This is different from the robustness to frequency offset, which aims to yield the same action on the resonance of interest over a range of frequency offsets, whereas the frequency selectivity aims to prevent unwanted excitation of other resonances. This selectivity is achieved by prescribing frequency regions by means of a weight function (W) with ideally 0 excitation, and the deviation from this ideal excitation profile is used to calculate a penalty term (Equation 8) for the final cost according to the norm defined in Equation 1.

$$penalty = W \bullet \| M_{z,simulated} - M_{z,ideal} \|_2^2. \quad (8)$$

This penalty term is indispensable where multiple resonances are of interest, especially with nonrenewable hyperpolarized signals. For example, in an experiment for which exchange of hyperpolarized ^{13}C label between [2-^{13}C]pyruvate and lactate is monitored, the lactate pulse should yield 0 excitation in the neighborhood of the pyruvate resonance in order to preserve the stored polarization in pyruvate. The Bloch simulation increased the total time of the cost function evaluation by 1%–3% (Figure 2C).

The frequency offsets and relative B_1 values (relative to the nominal B_1 value) used in the optimization process were [−200 Hz, 200 Hz] and [0.1, 3.3], with step-sizes of 100 Hz and 0.8, respectively. The cost function values were weighted according to Gaussians, with a FWHM of 400 Hz for the frequency offsets and a FWHM of 2 for the relative B_1 amplitudes.

3 | METHODS

Experiments were performed at 7 Tesla (Agilent, Palo Alto, CA) using home-built dual-tuned 2-cm diameter ^{1}H-^{13}C and ^{1}H-^{15}N transmit–receive surface coils. Phantom experiments were performed using thermally polarized 5M [1-^{13}C]lactate, 2M [2-^{13}C]lactate, and 1M [$^{15}N_2$]urea solutions. Spectra were acquired into 1024 complex points with a spectral bandwidth of 4006 Hz. In the polarization transfer experiments, the reference experiment, acquired without polarization transfer, used a 2 ms 90° type-4 B_1 -insensitive rotation (BIR4) adiabatic excitation pulse immediately followed by signal acquisition.

3.1 | Adiabatic INEPT pulse sequence

The adiabatic INEPT pulse sequence used for proton to carbon polarization transfer in the [1-^{13}C]lactate phantom is described in Ref. [14]. The transfer block employed 4 ms 90° sinc pulses and 10 ms hyperbolic secant (HS8) adiabatic refocusing pulses. The delay between the center of the first and second 90° pulses was 121.95 ms, and the delay

between the center of the second 90° pulse and the start of acquisition was 47.78 ms.

3.2 | BINEPT pulse sequence

The pulse sequence was implemented as described in Ref. [33]. The transfer block starts with 2 ms BIR4 pulses segmented into 0.5 ms–1 ms–0.5 ms subpulses. The 3 subpulses were separated by two 2.78 ms delays. The segmented pulse was followed by an evolution period of 2.78 ms, with a 2 ms 180° BIR4 pulse in the middle to refocus anti-phase magnetization.

3.3 | Partial transfer of polarization from hyperpolarized ^{15}N to protons

The [$^{15}N_2$]urea sample contained 45.9 mg [$^{15}N_2$]urea, 2.31 mg OXO63 trityl radical, 62.8 mg ^2H_2O, and 55.4 mg glycerol, and 37.5 mg was polarized for 3 hours in a Hypersense DNP Polarizer (Oxford Instruments, Abingdon, UK). Dissolution was performed in 6 mL ^2H_2O heated to 180°C and pressurized to 10 bar.[34] The pulse sequence used for ^{1}H detection of the hyperpolarized [$^{15}N_2$]urea employed a variable power radiofrequency pulses with optimized relaxation delays (VAPOR) water-suppression block in the vendor-provided PRESS sequence. Delays and RF amplitudes were optimized online with the built-in module of the water suppression block. The hyperpolarized sample was injected into a 2 mL Eppendorf-tube next to a thermally polarized 1M [$^{15}N_2$]urea phantom used for center frequency calibration. The dynamic acquisition was started immediately after injection.

3.4 | J-coupling modulation-free excitation of thermally polarized [2-^{13}C] lactate and [$^{15}N_2$]urea

Forty-five degree excitation pulses were designed to eliminate J-coupling modulation in [2-^{13}C]lactate (^{13}C doublet peak) and [$^{15}N_2$]urea (^{15}N triplet peak). Spectra were acquired into 1024 complex points with a spectral width of 4006 Hz. The spectra were compared to those obtained using a 100 μs hard pulse with matching flip angle.

3.5 | Imaging a [2-^{13}C]lactate phantom

Single-shot 3D non-Cartesian images were acquired using a 1-cm diameter ^{13}C transmit–receive surface coil (Agilent, Palo Alto, CA). Images were acquired using a multi-spin echo pulse sequence.[32] The FOV was 3.2 cm with a nominal image resolution of 2 mm. The excitation pulse was either a 2 ms 45° BIR4 pulse or the optimized pulse designed for elimination of J-coupling modulation. The 7 uniformly spaced spin echoes were generated using 12 ms hyperbolic secant (HS8) adiabatic refocusing pulses without slice selection, with a TE of 25.4 ms. The refocusing pulses were phase-compensated.[35] Readout band-width was set to 250 kHz. The sampled k-space was gridded to a twofold oversampled 32 × 32 × 32 3D Cartesian grid using a Kaiser-Bessel function with density pre- and postcompensation, followed by 3D inverse Fourier-transform and deapodisation. The same pulse sequence with a 2 ms 90° BIR4 excitation pulse was used for T_2 measurements with the readout gradients switched off. At each of the 7 spin echoes, 3157 complex points were acquired; and after Fourier-transform, the 7 peaks were fitted to a monoexponential decay function.

3.6 | Dynamic acquisition of J-coupling modulation-free spectra in vivo

A series of ^{13}C spectra were acquired from the brain of a BALB/c nude mouse (Charles River Laboratories, Wilmington, Massachusetts, US) following injection of 300 μL of 80 mM hyperpolarized [2-^{13}C]pyruvate. The acquisition started immediately after the start of injection. The experiment was carried out in compliance with a project and personal licenses issued by the Home Office, UK, and was approved by the Cancer Research UK, Cambridge Institute Animal Welfare and Ethical Review Body. The [2-^{13}C]pyruvate contained 44 mg [2-^{13}C]pyruvic acid (CIL, MA), 15 mM OX063 (GE Healthcare, Chalfont St. Giles, Buckinghamshire, UK), and 1.4 mM gadoterate meglumine (Dotarem; Guerbet, Roissy, France) and was polarized for 1 h. The sample was then rapidly dissolved in 6 mL buffer containing 40 mM HEPES, 94 mM NaOH, and 30 mM NaCl 100 mg/L EDTA heated to 180 °C and pressurized to 10 bar.

4 | RESULTS

4.1 | Polarization transfer from proton to carbon in [1-^{13}C]lactate

Polarization is transferred from the methyl protons to the ^{13}C nucleus (J = 4.1Hz). However, the methine proton is also coupled to both the methyl protons (J = 7 Hz) and to the carboxyl carbon (J = 3.2 Hz). The simulation was insensitive to the values of the ^{1}H and ^{13}C T_1 relaxation times;

therefore, published values were used: $T_1^{13C} = 50$ s (at 7 Tesla),[36] $T_1^{1H} = 1.73$ s (at 4.7 Tesla).[37] T_2 relaxation times were measured using a multi-spin echo sequence,[32] giving values of $T_2^{13C} = 1.625$ s and $T_2^{1H} = 463$ ms. The target state for the optimization was to place the ^{13}C magnetization in-phase in the *x*–*y* plane immediately after polarization transfer. The resultant spectrum was compared to spectra obtained without polarization transfer and using the pulse sequence described in Ref. [14], which employed adiabatic refocusing pulses in a refocused INEPT experiment (Figure 3B). The SNR of the optimized experiment was 1.41 ± 0.19 times higher compared to detection without polarization transfer and 1.29 ± 0.17 times higher than in the INEPT experiment. The simulated SNR improvement of the optimized sequence relative to detection without polarization transfer was 1.42.

4.2 | Polarization transfer from proton to carbon in [2-^{13}C]lactate

Polarization is transferred from the methine proton to the ^{13}C nucleus (J = 140 Hz). However, the methyl protons are also coupled to both the methine proton (J = 7 Hz)

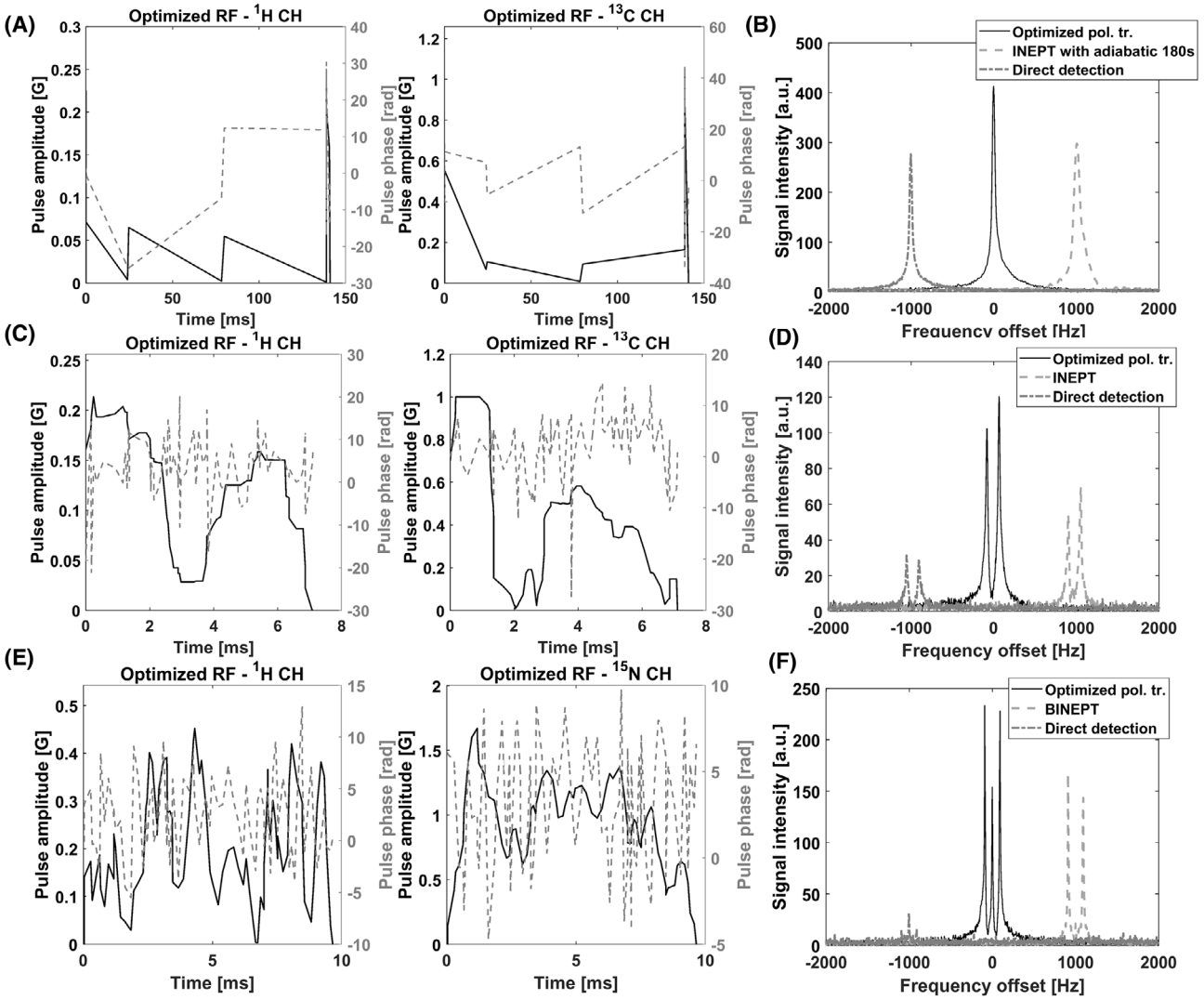

FIGURE 3 (A) Optimized pulses for transfer of ^{1}H polarization to ^{13}C in [1-^{13}C]lactate. (B) Comparison of the spectrum acquired with the optimized sequence to the spectra acquired with the adiabatic insensitive nuclei enhanced by polarization transfer (INEPT) sequence described in Ref. [14] and by detection without polarization transfer (direct ^{13}C detection). The latter spectra are shifted by ±1000 Hz. (C) Optimized pulses for transfer of ^{1}H polarization to ^{13}C in [2-^{13}C]lactate. (D) Comparison of the spectrum acquired with the optimized sequence to that acquired without polarization transfer (direct ^{13}C detection). (E) Optimized pulses for transfer of ^{1}H polarization from the pairs of ^{1}H nuclei to the ^{15}N nuclei in [^{15}N]urea. (F) Comparison of the spectrum acquired with the optimized sequence to that acquired using the B_1 -insensitive heteronuclear adiabatic polarization transfer (BINEPT) sequence and by detection without polarization transfer (direct ^{15}N detection). The latter spectra are shifted by ±1000 Hz

and to the C2 carbon (J = 4.2 Hz). Because use of the exact relaxation time values is not critical in cases in which the J-coupling constant is large, the simulation was run with the ^{1}H and ^{13}C T_2, and the ^{1}H T_1 relaxation times used for [1-^{13}C]lactate. The ^{13}C T_1 (T_1^{13C}) was set to 7.2 s.[38] The target for the optimization was to place the ^{13}C magnetization in-phase in the *x*–*y* plane immediately after polarization transfer. The resultant spectrum was compared with the spectrum obtained by detection without polarization transfer and with the conventional INEPT sequence, which used 1-ms hard pulses (Figure 3D). Adiabatic INEPT sequences could not be used due to the relatively long adiabatic pulses (2–10 ms) when compared to the short interpulse delays in the polarization transfer sequence, which are the result of the large coupling constant between the methine proton and C2 carbon. The SNR of the optimized experiment was 3.81 ± 0.83 times higher compared to detection without polarization transfer and 1.91 ± 0.67 higher compared to the INEPT sequence. The theoretical maximum for the transfer of proton polarization to ^{13}C is $\gamma_{1H}/\gamma_{13C} = 3.97$, when neglecting the other much weaker couplings and relaxation. The insensitivity of the ^{13}C signal to variation in the ^{13}C and ^{1}H B_0 and B_1 fields in the optimized experiment was demonstrated by sweeping the ^{13}C and ^{1}H center frequencies and changing the transmitter gains. The results obtained were compared with those obtained using the hard pulse INEPT sequence (Figure 4).

4.3 | Polarization transfer from proton to nitrogen in [$^{15}N_2$]urea

Polarization is transferred from the 2 pairs of magnetically equivalent protons to each of the two ^{15}N nuclei (J = −90 Hz). The optimization used the measured values for ^{1}H and ^{15}N relaxation times from Ref. [15], $T_2^{15N} = 1.62$ s, $T_2^{1H} = 60$ ms, $T_1^{15N} = 24.2$ s, and $T_1^{1H} = 2.57$ s. The SNR of the ^{15}N triplet with the optimized sequence was 1.66 ± 0.20 and 9.96 ± 1.83 times higher than that obtained using the B_1-insensitive heteronuclear adiabatic polarization transfer (BINEPT) pulse sequence and detection without polarization transfer, respectively (Figure 3F). The optimized sequence better preserved the multiplet structure, which may be lost in the BINEPT sequence due to antiphase magnetization resulting from the relatively long adiabatic pulses. The optimized sequence required a more than twofold lower peak B_1 compared to the BINEPT sequence.

4.4 | Polarization transfer from hyperpolarized nitrogen to protons in [$^{15}N_2$]urea

In order to allow serial acquisition of spectra, polarization has to be transferred from the hyperpolarized ^{15}N nuclei to the coupled protons in discrete packets.[15]

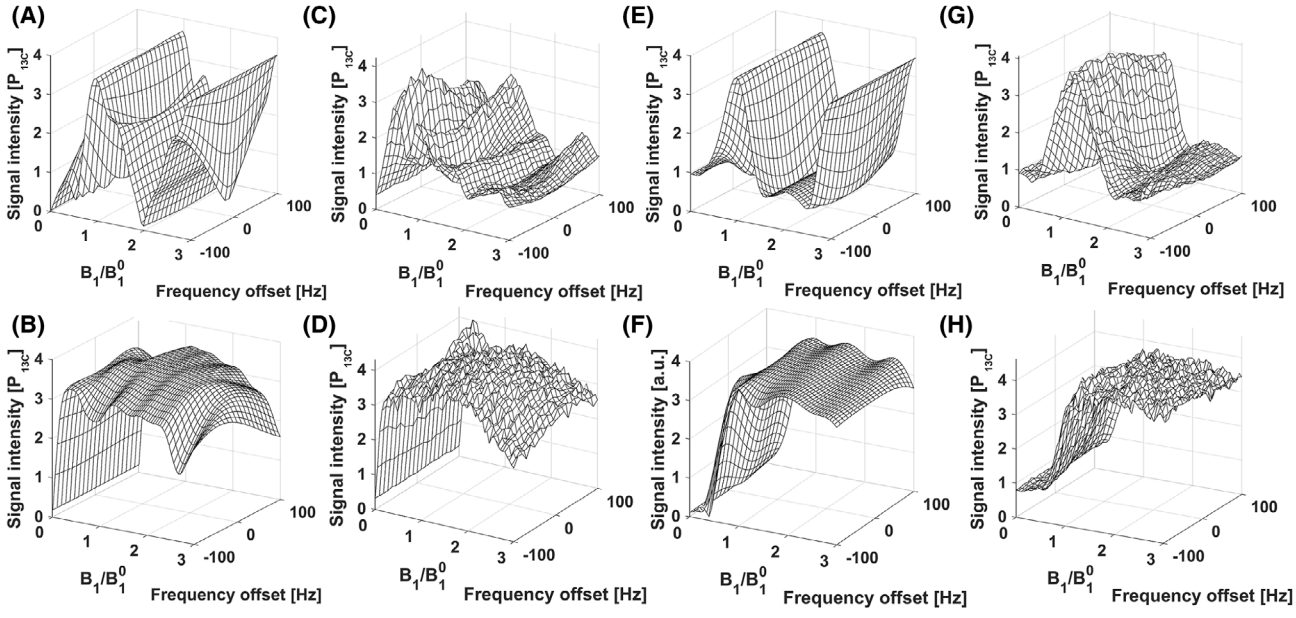

FIGURE 4 Simulated and measured signal intensity of the ^{13}C resonance in the [2-^{13}C]lactate phantom after transferring polarization from the spin coupled C2 proton. The results are normalized to the equilibrium ^{13}C polarization. Results obtained using the hard pulse INEPT sequence (A,C,E,G) and the optimized pulse (B,D,F,H) are compared. A,B,E and F show simulated profiles and C,D,G and H show those determined experimentally. A–D show the effects of varying the ^{13}C offset and transmitter gain and E–H show the effects of varying the ^{1}H offset and transmitter gain. The data were acquired at 7T with the dual-tuned ^{1}H-^{13}C surface coil

Simulations showed ΔB_0 and ΔB_1 robustness comparable to the IRRUPT pulse sequence,[15] which is a partial transfer version of the BINEPT sequence (Figure 5A). Signal was observable for up to 24 s (12 repetitions) even though injection of the hyperpolarized urea solution significantly degraded B_0 homogeneity (Figure 5C). The required B_1 amplitude for this optimized sequence was approximately twofold lower than that needed for the IRRUPT sequence.

4.5 | Pulses immune to the effects of J-coupling in [2-^{13}C]lactate and [$^{15}N_2$]urea

An optimized ^{13}C pulse (Figure 6A) designed to yield a 45° excitation of the upfield peak in the [2-^{13}C]lactate doublet (Figure 6B) and minimal excitation of the pyruvate and pyruvate–hydrate resonances (Figure 6C) took only 9.76 ms. The algorithm finds the shortest pulse that minimizes signal loss but can still perform selection of the singlet component over the prescribed range of resonance frequency offsets. The pulse, which is applied at the center frequency of the ^{13}C doublet, steers the ^{13}C magnetization to a final state, where there is an equal mixture of in-phase and anti-phase ^{13}C magnetization. A better selectivity was observed between the frequency offsets of interest at $+J/2 = 70$ Hz and $-J/2 = -70$ Hz when compared with a 32 ms hard pulse and a 10 ms sinc pulse applied at the resonance frequency of 1 of the components of the doublet ($+J/2 = 70$ Hz), as described in Ref. [18] (Figure 7). A similar excitation pulse was designed for J-coupling artefact-free imaging of the triplet resonance from [$^{15}N_2$] urea. The analytical derivation is complicated even for a system of 2 coupled spins[18] and does not hold for a system of 3 or more spins. For the numerical optimization approach, it is sufficient simply to define the desired state of the spin system immediately after excitation as that containing a singlet peak. This is a mixture of in-phase (e.g., $\hat{I}_x$, $\hat{I}_y$ etc.) and certain anti-phase (e.g., $\hat{I}_x\hat{S}_z$, $\hat{I}_y\hat{S}_z$ etc.) magnetization terms so that the other components of the multiplet cancel. This is trivial to find and constitutes the input for the optimization. For example, the desired state is $\hat{\rho} = (a_x I_x + a_y I_y) + 2(a_x I_x + a_y I_y) S_z^{CH}$ for the ^{13}C doublet case and $\hat{\rho} = (b_x I_x + b_y I_y) - 4(b_x I_x + b_y I_y) S_{1z} S_{2z}$ for the ^{15}N triplet. The coefficients a_x, a_y, b_x, b_y are arbitrary real numbers such that $\hat{\rho}$ obeys density matrix normalization rules. They also indicate that the final phase

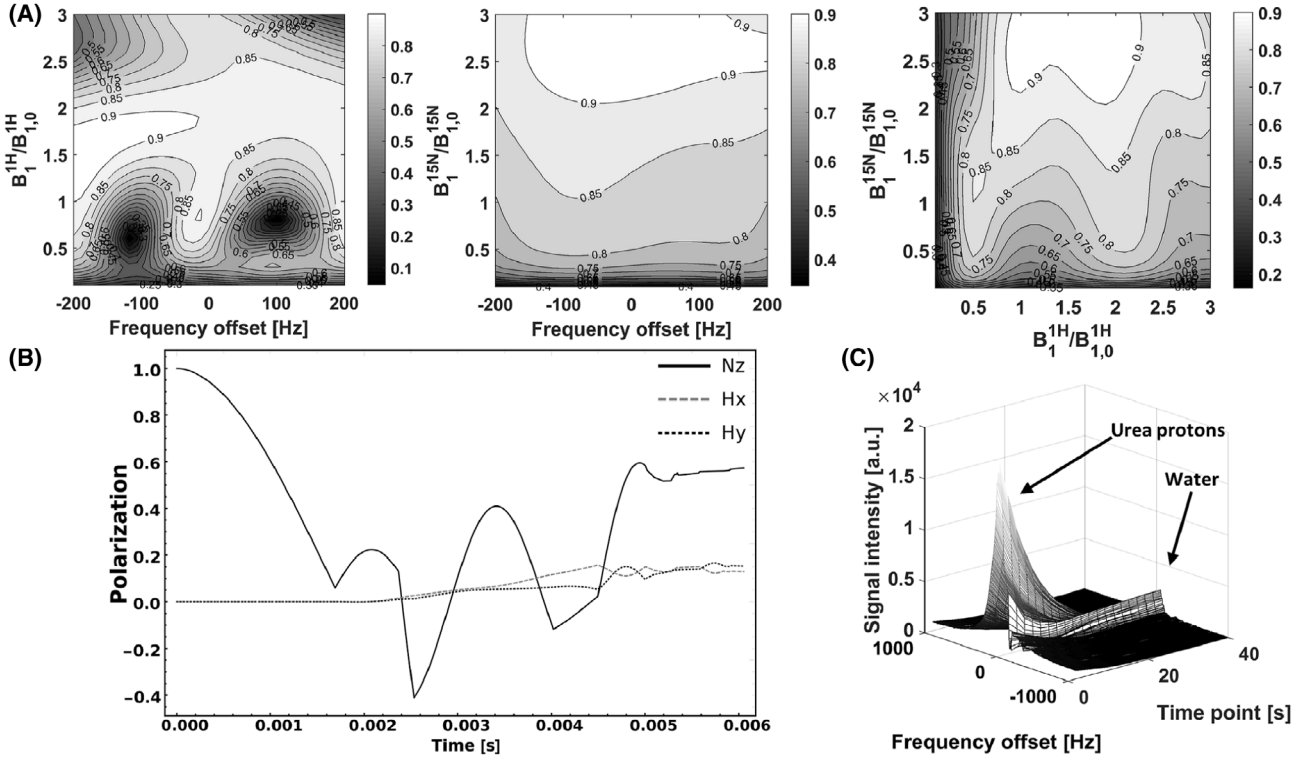

FIGURE 5 (A) Simulated efficiency of partial polarization transfer from ^{15}N to ^{1}H in [$^{15}N_2$]urea, defined as $P_{transfered}/(1-P_{preserved})$. (B) Evolution of the ^{1}H and ^{15}N magnetizations. (C) Time course of polarization transfer from hyperpolarized ^{15}N to protons in a [$^{15}N_2$]urea phantom. The broad urea peak is the result of the degraded magnetic field homogeneity caused by injection of the hyperpolarized [$^{15}N_2$]urea solution. The residual water peak is the result of inadequate water suppression

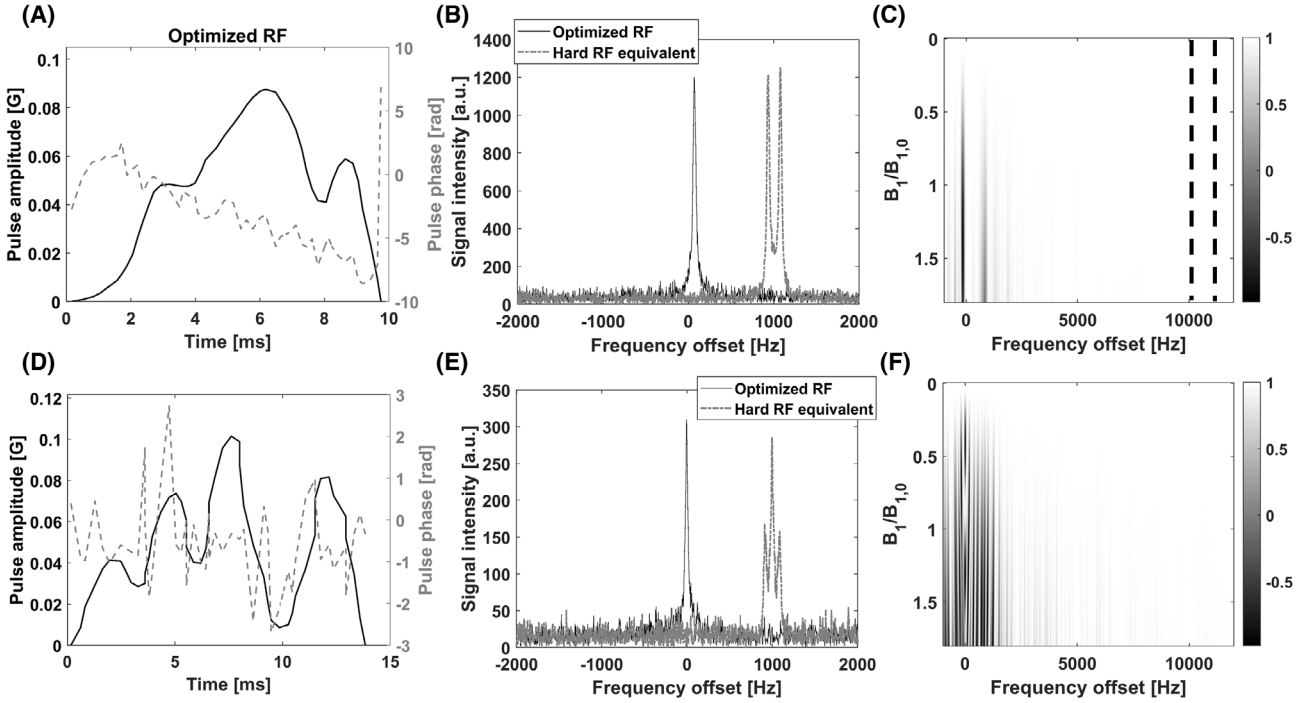

FIGURE 6 (A) An optimized 45° ^{13}C excitation pulse for artefact-free imaging of [2-^{13}C] lactate (J = 140 Hz). (B) The resultant spectrum compared with that acquired with an equivalent hard pulse. The latter was shifted by 1000 Hz. (C) The Bloch-simulated ^{13}C z-magnetization immediately after the pulse. The dashed lines indicate the ±200 Hz region containing the [2-^{13}C]pyruvate resonance, where the pulse gave minimal excitation. (D) An optimized excitation pulse for [$^{15}N_2$]urea. (E) The resultant spectrum compared with that acquired with an equivalent hard pulse, which showed the proton-coupled triplet. (F) The Bloch-simulated ^{15}N z-magnetization immediately after the pulse

of the spectrum relative to the receiver is unimportant, but it needs to be same for the in-phase and anti-phase terms so that the respective components of the multiplets cancel. It is important to note here that the anti-phase terms relax according to the sum of the relaxation rates of the individual spin operator components. The optimization used the T_1 and T_2 values for [2-^{13}C]lactate and [$^{15}N_2$]urea given above. The optimized excitation pulse for [$^{15}N_2$]urea and the resultant singlet spectrum are shown in Figure 6D,E, respectively. The pulse was longer, at 13.84 ms, reflecting the smaller J-coupling and therefore slower spin evolution. The ^{13}C pulse was used for single-shot 3D imaging of the lactate phantom using a multi-spin echo readout.[32] The image acquired with the optimized excitation pulse showed only readout point spread function-associated artefacts, whereas the image acquired using a BIR4 excitation pulse introduced blurring and image distortion originating from J-coupling dependent modulation of the ^{13}C signals (Figure 8). A series of ^{13}C spectra acquired from the rat brain following intravenous injection of hyperpolarized [2-^{13}C]pyruvate using the same optimized pulse contained only the upfield peak of the [2-^{13}C]lactate doublet, which was observable for up to 40 s. The spectra showed no detectable pyruvate or pyruvate-hydrate signal (Figure 9).

5 | DISCUSSION

Metabolic imaging using hyperpolarized ^{13}C-labeled substrates has provided a new tool for investigating tissue metabolism in vivo[39–42] and has translated to the clinic with studies in oncology[43–47] and cardiology.[48–51] Despite the enormous gain in sensitivity,[31] there has, nevertheless, been attempts to further improve sensitivity by transferring polarization from nuclei such as ^{13}C and ^{15}N, in which the polarization is long-lived, to protons. A reverse INEPT sequence has been used for ^{1}H imaging of [1-^{13}C]lactate in vivo following injection of hyperpolarized [1-^{13}C]pyruvate.[14,16] However, the use of adiabatic pulses, which allowed its implementation in vivo using a surface coil, required a compromise to be made between the frequency selectivity of these pulses and their robustness to B_1 inhomogeneity. Polarization transfer efficiency can also be reduced by longer adiabatic pulses, which is particularly severe when there is strong J coupling and the polarization transfer element of the pulse sequence is consequently much shorter.[15] The high-energy deposition and peak B_1 amplitude of adiabatic pulses is also a problem for clinical translation.

The pulse sequences generated using the optimization approach described here showed improved performance in transferring polarization from protons to X nuclei

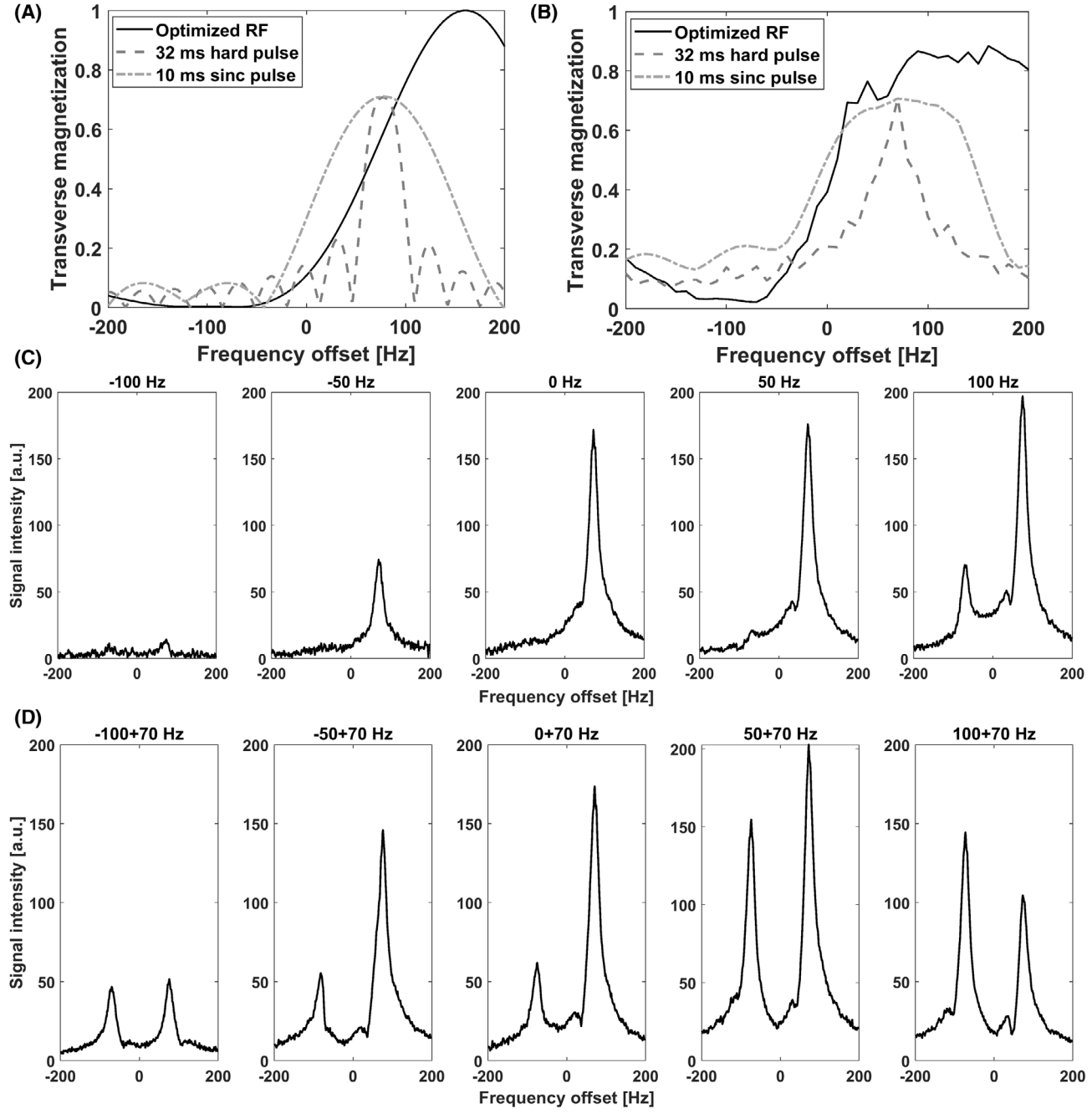

FIGURE 7 (A) Simulated frequency profile of the 9.76 ms optimized RF pulse designed to give J-coupling artefact-free excitation of [2-^{13}C]lactate when the pulse is applied exactly on-resonance at the center frequency of the ^{13}C doublet. The profile is compared to that of a +J/2 = 70 Hz off-resonant 32 ms hard pulse and a 10 ms sinc pulse. (B) The same profiles measured experimentally. (C) ^{13}C spectra acquired from [2-^{13}C]lactate with the optimized pulse at different offset values of the doublet center frequency. (D) ^{13}C spectra acquired from [2-^{13}C] lactate with the 10-ms sinc pulse applied at +70 Hz from different offset values of the doublet center frequency

when compared with the INEPT sequence and its adiabatic variants. These experiments should show a similarly improved performance in transferring polarization from hyperpolarized X nuclei to protons when compared to a reverse INEPT experiment. The INEPT transfer efficiency decreases due to field imperfections, finite pulse lengths, and relaxation. The latter is an issue with small coupling constants, for example, the 4.1 Hz coupling between the C1 carbon and methyl protons in [1-^{13}C]lactate. Nevertheless, proton detection of hyperpolarized [1-^{13}C]lactate still improved the SNR.[14] However, to achieve an acceptable specific absorption rate (SAR) for proton detection of [1-^{13}C] lactate on a 3 Tesla clinical scanner would require a minimum TR of 10 s, which would result in a considerable loss of dynamic information. The SAR of the optimized pulse sequence was 2.3 times lower. Furthermore, the

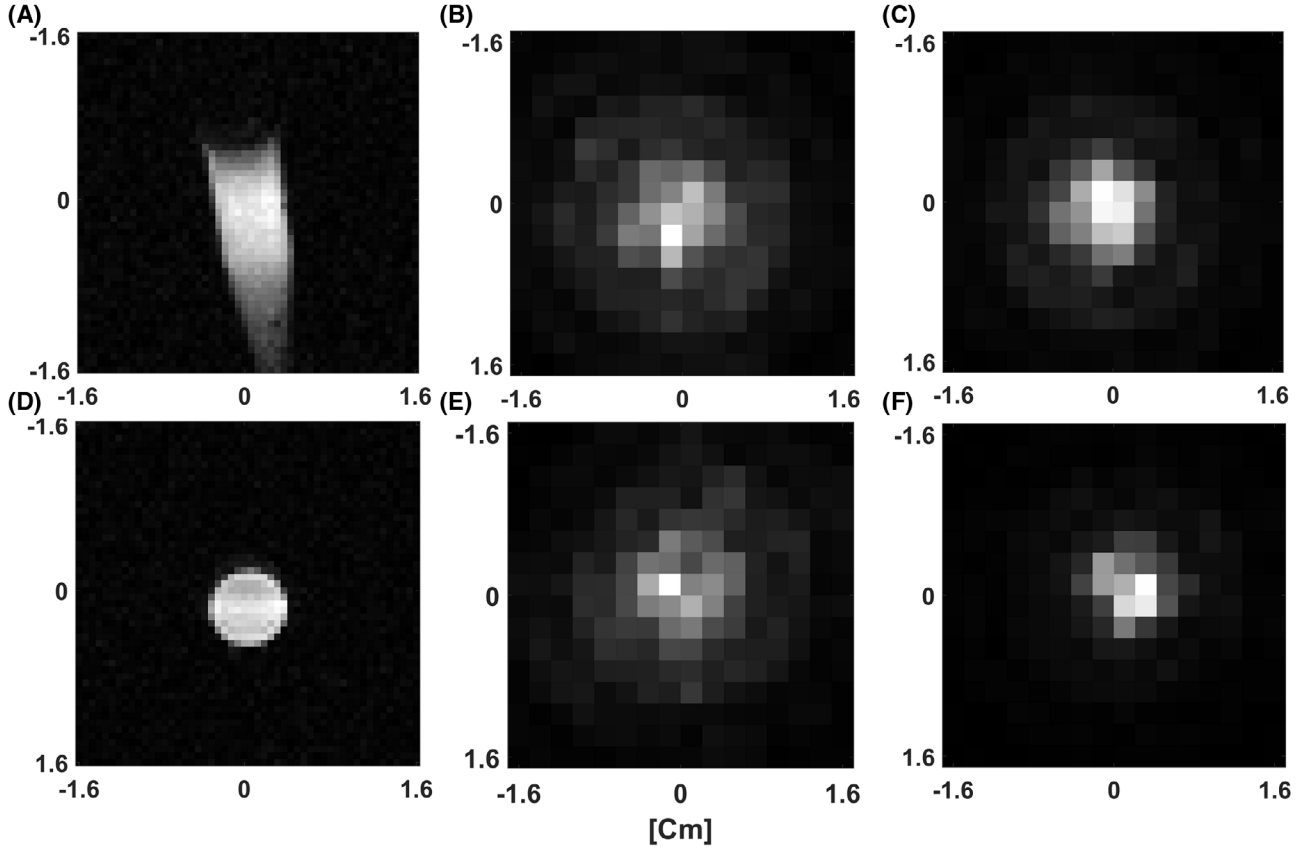

FIGURE 8 Single-shot 3D imaging of a [2-^{13}C]lactate phantom. (A) and (D) are central sagittal and axial ^{1}H images respectively acquired using a fast spin echo sequence. (B), (E) The corresponding ^{13}C images acquired with the pulse sequence described in Ref. [32] using an adiabatic 45° BIR4 excitation pulse. (C), (F) The same images acquired using the optimized excitation pulse shown in Figure 6A

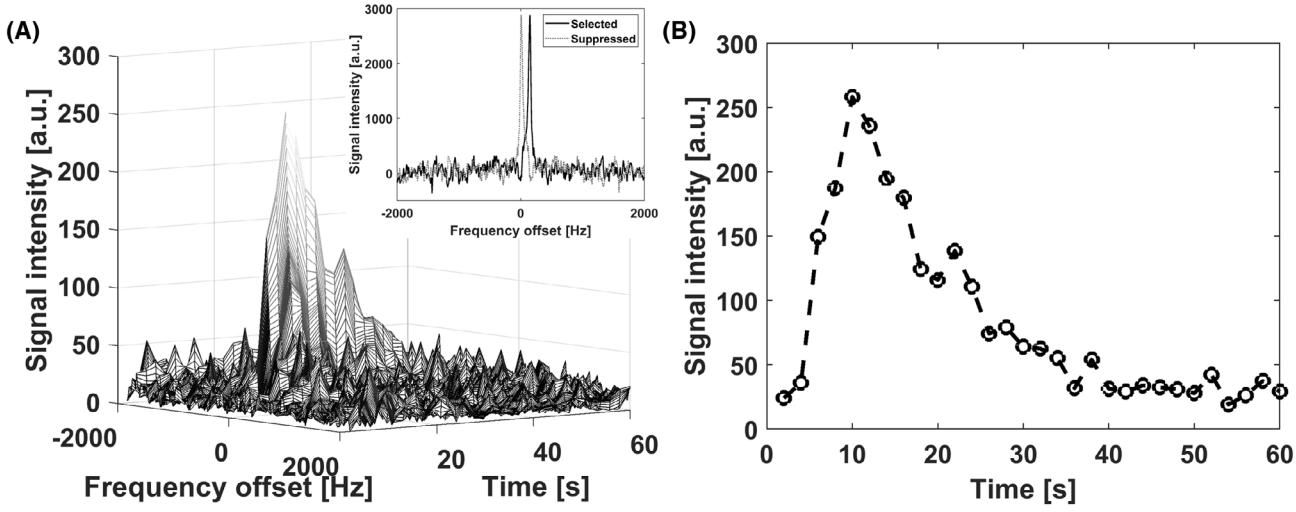

FIGURE 9 (A) ^{13}C spectra acquired from a mouse brain following injection of hyperpolarized [2-^{13}C]pyruvate. The inset displays the sum of the acquired spectra (solid line) and the doublet component (dotted line) that would have been obtained without the optimized pulse, which is based on the linewidth and frequency offset of the observed singlet. The excitation pulse was designed to give J-modulation–free imaging of [2-^{13}C]lactate. (B) Time-course of the singlet peak intensity

hyperbolic secant (HS8) refocusing pulses used in this sequence also have a high adiabatic threshold, which may not be achievable on a clinical scanner. The same problem exists for BIR4 pulses. Both BIR4 and HS8 are relatively long, which significantly reduces polarization transfer efficiency when the coupling constants are large. When compared to a polarization transfer sequence that allows serial partial transfers of polarization (IRRUPT),[15] the

optimized sequence showed a similar performance but required a much lower peak B_1 field, and therefore had a lower SAR. For example, the maximum B_1 field for a clinical coil is usually less than 1 G for ^{13}C, whereas a typical BIR4 pulse used in the IRRUPT sequence has an adiabatic threshold of several G. Also, the BIR4 pulse, and therefore the IRRUPT sequence, are not frequency-selective.

Removal of 1 component of the [2-^{13}C]lactate doublet, either by using a frequency-selective pulse on the other component[18] or the optimized pulse described here applied at the center frequency of the doublet, is achieved in both cases through phase cancelation. However, the 9.76-ms optimized pulse shows a comparable bandwidth to the 10-ms sinc pulse and a much wider bandwidth than 32-ms hard pulse at the frequency of the observed component but, importantly, much less signal from the other component than that observed with either the hard or sinc pulses. Effective removal of 1 of the components of the doublet using the optimized pulse was demonstrated in the phantom images and in the spectra acquired in vivo.

A limitation of the optimization process is the slow speed of convergence, typical of genetic algorithms. In combination with the computational complexity of the spin dynamics simulation in the cost function, the optimization process is limited to small spin systems. However, the hyperpolarized substrates that are of interest in MR metabolic imaging experiments are often small, frequently no more than 5 coupled spins.[52,53] Furthermore, if the coupling of interest is significantly stronger than the others, the further spin–spin pairs can be neglected. Even in the case of larger molecules, the coupling networks are usually short-range, and the scale of simulation can be reduced by means of state–space restriction techniques. The waveform smoothing technique and the approximation applied in the spin dynamics simulation (Equation 8) also markedly decreased the required computational time. A limitation of the approximation (Equation 8) is that accounting for cross-relaxation and other nondiagonal terms in the relaxation model is not straightforward. Nevertheless, the proposed method could have general applications in studies in which a hyperpolarized X nucleus is monitored[40,54–60] and the detection via spin-coupled protons is expected to result in an enhanced SNR. The optimization process could also be employed in the design of excitation and refocusing pulses with prescribed frequency profiles, both with[6] and without[61,62] the presence of J-coupling modulation. The full Bloch simulation in the cost function also allows the optimal design of selective excitation pulses for UTE MRI.[63–65] A potential extension would be to include gradient channels in the optimization. This would enable, for example, the optimized design of spectral–spatial pulses, water-suppression sequences, and diffusion-encoding blocks and it is expected to be computationally tractable. However, incorporating gradients into the spin dynamics simulation, for example, for coherence selection, is anticipated to increase significantly the runtime of the cost function evaluation.

6 | CONCLUSION

In conclusion, the proposed optimization method provides a simple framework for the design of pulse sequences that are robust to the effects of B_1 and B_0 inhomogeneity, typical for in vivo experiments, and reduce energy deposition and therefore could facilitate clinical translation of preclinical imaging sequences.

ACKNOWLEDGMENT

The authors acknowledge the support of the Cancer Research UK Cambridge Institute biological resources unit and preclinical imaging core facilities. We would like to thank Mike Mitchell and Toby Fewster for their help. This work was funded by the European Union's Horizon 2020 Research and Innovation Program under FETOPEN grant agreement no. 858149 (AlternativesToGd) and Cancer Research UK Grants (C197/A16465, C55296/A26605, C9685/A25177). v.s. and f.h. are in receipt of a Cambridge European Scholarship from the Cambridge Trust.

CONFLICT OF INTEREST

K.M.B. has a research agreement with GE Healthcare and holds patents with them on some aspects of DNP technology. k.m.b. also has recently (since this paper was submitted) entered into a consultancy agreement with NVision Imaging Technologies GmbH who are developing hyperpolarization technology.

DATA AVAILABILITY STATEMENT

All design code is available at: https://github.com/vs460/PulseSequenceOptimization.git

ORCID

Vencel Somai https://orcid.org/0000-0001-9874-526X
Alan J. Wright https://orcid.org/0000-0002-4577-5681
Kevin M. Brindle https://orcid.org/0000-0003-3883-6287

REFERENCES

1. Khaneja N, Reiss T, Kehlet C, Schulte-Herbrüggen T, Glaser SJ. Optimal control of coupled spin dynamics: design of NMR pulse sequences by gradient ascent algorithms. *J Magn Reson*. 2005;172:296-305.
2. Manu VS, Kumar A. Singlet-state creation and universal quantum computation in NMR using a genetic algorithm. *Phys Rev A*. 2012;86:022324.

3. Manu VS, Kumar A. Quantum simulation using fidelity-profile optimization. *Phys Rev A*. 2014;89:052331.
4. Subrahmanian MV, Dregni AJ, Veglia G. Optimal design of offset-specific radio frequency pulses for solution and solid-state NMR using a genetic algorithm. In: Webb GA, ed., *Modern Magnetic Resonance*. 2nd ed. Springer International Publishing; 2018:605-615.
5. Tošner Z, Vosegaard T, Kehlet C, Khaneja N, Glaser SJ, Nielsen NC. Optimal control in NMR spectroscopy: numerical implementation in SIMPSON. *J Magn Reson*. 2009;197:120-134.
6. Manu VS, Veglia G. Genetic algorithm optimized triply compensated pulses in NMR spectroscopy. *J Magn Reson*. 2015;260:136-143.
7. Ladd TD, Jelezko F, Laflamme R, Nakamura Y, Monroe C, O'Brien JL. Quantum computers. *Nature*. 2010;464:45-53.
8. Brif C, Chakrabarti R, Rabitz H. Control of quantum phenomena: past, present and future. *New J Phys*. 2010;12:075008.
9. Motzoi F, Gambetta JM, Rebentrost P, Wilhelm FK. Simple pulses for elimination of leakage in weakly nonlinear qubits. *Phys Rev Lett*. 2009;103:110501.
10. Glaser SJ, Boscain U, Calarco T, et al. Training Schrödinger's cat: quantum optimal control. *Eur Phys J D*. 2015;69:279.
11. Hogben HJ, Krzystyniak M, Charnock GTP, Hore PJ, Kuprov I. Spinach—a software library for simulation of spin dynamics in large spin systems. *J Magn Reson*. 2011;208:179-194.
12. Coote PW, Robson SA, Dubey A, et al. Optimal control theory enables homonuclear decoupling without Bloch-Siegert shifts in NMR spectroscopy. *Nat Commun*. 2018;9:3014.
13. Holland JH. *Adaptation in Natural and Artificial Systems*. University of Michigan Press; 1975.
14. Wang J, Kreis F, Wright AJ, Hesketh RL, Levitt MH, Brindle KM. Dynamic ^{1}H imaging of hyperpolarized [1-^{13}C]lactate in vivo using a reverse INEPT experiment. *Magn Reson Med*. 2018;79:741-747.
15. Kreis F, Wright AJ, Somai V, Katz-Brull R, Brindle KM. Increasing the sensitivity of hyperpolarized [$^{15}N_2$]urea detection by serial transfer of polarization to spin-coupled protons. *Magn Reson Med*. 2020;84:1844-1856.
16. von Morze C, Reed GD, Larson PE, et al. In vivo hyperpolarization transfer in a clinical MRI scanner. *Magn Reson Med*. 2018;80:480-487.
17. Morris GA, Freeman R. Enhancement of nuclear magnetic resonance signals by polarization transfer. *J Am Chem Soc*. 1979;101:760-762.
18. Datta K, Spielman D. MRI of [2-^{13}C]Lactate without J-coupling artifacts. *Magn Reson Med*. 2021;85:1522-1539.
19. Chauffert N, Weiss P, Kahn J, Ciuciu P. A projection algorithm for gradient waveforms design in magnetic resonance imaging. *IEEE Trans Med Imaging*. 2016;35:2026-2039.
20. Ernst RR, Bodenhausen G, Wokaun A. *Principles of Nuclear Magnetic Resonance in One and Two Dimensions*. Clarendon Press; 1987.
21. Levitt MH, Di Bari L. The homogeneous master equation and the manipulation of relaxation networks. *Bull Magn Reson*. 1994;16:94-114.
22. Bengs C, Levitt MH. A master equation for spin systems far from equilibrium. *J Magn Reson*. 2020;310:106645.
23. Kuprov I, Wagner-Rundell N, Hore PJ. Polynomially scaling spin dynamics simulation algorithm based on adaptive state-space restriction. *J Magn Reson*. 2007;189:241-250.
24. Hogben HJ, Hore PJ, Kuprov I. Strategies for state space restriction in densely coupled spin systems with applications to spin chemistry. *J Chem Phys*. 2010;132:174101.
25. Karabanov A, Kuprov I, Charnock GTP, Van Der Drift A, Edwards LJ, Köckenberger W. On the accuracy of the state space restriction approximation for spin dynamics simulations. *J Chem Phys*. 2011;135:084106.
26. Krzystyniak M, Edwards LJ, Kuprov I. Destination state screening of active spaces in spin dynamics simulations. *J Magn Reson*. 2011;210:228-232.
27. Kuprov I. Diagonalization-free implementation of spin relaxation theory for large spin systems. *J Magn Reson*. 2011;209:31-38.
28. Edwards LJ, Savostyanov DV, Welderufael ZT, Lee D, Kuprov I. Quantum mechanical NMR simulation algorithm for protein-size spin systems. *J Magn Reson*. 2014;243:107-113.
29. Kuprov I. Polynomially scaling spin dynamics II: further state-space compression using Krylov subspace techniques and zero track elimination. *J Magn Reson*. 2008;195:45-51.
30. Bain AD, Anand CK, Nie Z. Exact solution to the Bloch equations and application to the Hahn echo. *J Magn Reson*. 2010;206:227-240.
31. Ardenkjaer-Larsen JH, Fridlund B, Gram A, et al. Increase in signal-to-noise ratio of >10,000 times in liquid-state NMR. *Proc Natl Acad Sci U S A*. 2003;100:10158-10163.
32. Somai V, Wright AJ, Fala M, Hesse F, Brindle KM. A multi spin echo pulse sequence with optimized excitation pulses and a 3D cone readout for hyperpolarized ^{13}C imaging. *Magn Reson Med*. 2020;84:1895-1908.
33. Merkle H, Wei H, Garwood M, Uğurbil K. B_1-insensitive heteronuclear adiabatic polarization transfer for signal enhancement. *J Magn Reson*. 1992;99:480-494.
34. Harris T, Gamliel A, Uppala S, et al. Long-lived ^{15}N hyperpolarization and rapid relaxation as a potential basis for repeated first pass perfusion imaging—marked effects of deuteration and temperature. *ChemPhysChem*. 2018;19:2148–2152.
35. Conolly S, Nishimura D, Macovski A. A selective adiabatic spin-echo pulse. *J Magn Reson*. 1989;83:324-334.
36. Wang J, Hesketh RL, Wright AJ, Brindle KM. Hyperpolarized ^{13}C spectroscopic imaging using single-shot 3D sequences with unpaired adiabatic refocusing pulses. *NMR Biomed*. 2018;31:e4004.
37. Luo Y, Rydzewski J, de Graaf RA, Gruetter R, Garwood M, Schleich T. In vivo observation of lactate methyl proton magnetization transfer in rat C6 glioma. *Magn Reson Med*. 1999;41:676-685.
38. Taglang C, Korenchan DE, von Morze C, et al. Late-stage deuteration of ^{13}C-enriched substrates for T_1 prolongation in hyperpolarized ^{13}C MRI. *Chem Commun*. 2018;54:5233-5236.
39. Brindle KM. Imaging metabolism with hyperpolarized ^{13}C-labeled cell substrates. *J Am Chem Soc*. 2015;137:6418-6427.
40. Wang ZJ, Ohliger MA, Larson PEZ, et al. Hyperpolarized ^{13}C MRI: state of the art and future directions. *Radiology*. 2019;291:273-284.
41. Adamson EB, Ludwig KD, Mummy DG, Fain SB. Magnetic resonance imaging with hyperpolarized agents: methods and applications. *Phys Med Biol*. 2017;62:R81-R123.
42. Serrao EM, Brindle KM. Potential clinical roles for metabolic imaging with hyperpolarized [1-^{13}C]pyruvate. *Front Oncol*. 2016;6:59.

43. Brindle K. Watching tumours gasp and die with MRI: the promise of hyperpolarised ^{13}C MR spectroscopic imaging. *Br J Radiol*. 2012;85:697-708.
44. Day SE, Kettunen MI, Gallagher FA, et al. Detecting tumor response to treatment using hyperpolarized ^{13}C magnetic resonance imaging and spectroscopy. *Nat Med*. 2007;13:1382-1387.
45. Albers MJ, Bok R, Chen AP, et al. Hyperpolarized ^{13}C lactate, pyruvate, and alanine: noninvasive biomarkers for prostate cancer detection and grading. *Cancer Res*. 2008;68:8607-8615.
46. Golman K, in 't Zandt R, Thaning M. Real-time metabolic imaging. *Proc Natl Acad Sci U S A*. 2006;103:11270-11275.
47. Asghar Butt S, Søgaard LV, Ardenkjaer-Larsen JH, et al. Monitoring mammary tumor progression and effect of tamoxifen treatment in MMTV-PymT using MRI and magnetic resonance spectroscopy with hyperpolarized [1-^{13}C]pyruvate. *Magn Reson Med*. 2015;73:51-58.
48. Miller JJ, Lau AZ, Teh I, et al. Robust and high resolution hyperpolarized metabolic imaging of the rat heart at 7T with 3D spectral-spatial EPI. *Magn Reson Med*. 2016;75:1515-1524.
49. Golman K, Petersson JS, Magnusson P, et al. Cardiac metabolism measured noninvasively by hyperpolarized ^{13}C MRI. *Magn Reson Med*. 2008;59:1005-1013.
50. Cavallari E, Carrera C, Sorge M, et al. The ^{13}C hyperpolarized pyruvate generated by ParaHydrogen detects the response of the heart to altered metabolism in real time. *Sci Rep*. 2018;8:8366.
51. Rider Oliver J, Apps A, Miller Jack JJJ, et al. Noninvasive in vivo assessment of cardiac metabolism in the healthy and diabetic human heart using hyperpolarized ^{13}C MRI. *Circ Res*. 2020;126:725-736.
52. Hesketh RL, Brindle KM. Magnetic resonance imaging of cancer metabolism with hyperpolarized ^{13}C-labeled cell metabolites. *Curr Opin Chem Biol*. 2018;45:187-194.
53. Brindle KM, Bohndiek SE, Gallagher FA, Kettunen MI. Tumor imaging using hyperpolarized ^{13}C magnetic resonance spectroscopy. *Magn Reson Med*. 2011;66:505-519.
54. Gallagher FA, Woitek R, McLean MA, et al. Imaging breast cancer using hyperpolarized carbon-13 MRI. *Proc Natl Acad Sci U S A*. 2020;117:2092-2098.
55. Chung BT, Chen H-Y, Gordon J, et al. First hyperpolarized [2-^{13}C]pyruvate MR studies of human brain metabolism. *J Magn Reson*. 2019;309:2-13.
56. Chen H-Y, Aggarwal R, Bok RA, et al. Hyperpolarized ^{13}C-pyruvate MRI detects real-time metabolic flux in prostate cancer metastases to bone and liver: a clinical feasibility study. *Prostate Cancer Prostatic Dis*. 2020;23:269-276.
57. Laustsen C, Nielsen PM, Qi H, Løbner MH, Palmfeldt J, Bertelsen LB. Hyperpolarized [1,4–^{13}C]fumarate imaging detects microvascular complications and hypoxia mediated cell death in diabetic nephropathy. *Sci Rep*. 2020;10:4-13.
58. Guglielmetti C, Najac C, Didonna A, Van der Linden A, Ronen SM, Chaumeil MM. Hyperpolarized ^{13}C MR metabolic imaging can detect neuroinflammation in vivo in a multiple sclerosis murine model. *Proc Natl Acad Sci U S A*. 2017;114:E6982-E6991.
59. MacKenzie JD, Yen YF, Mayer D, Tropp JS, Hurd RE, Spielman DM. Detection of inflammatory arthritis by using hyperpolarized ^{13}C-pyruvate with MR imaging and spectroscopy. *Radiology*. 2011;259:414-420.
60. Sriram R, Nguyen J, Santos JD, et al. Molecular detection of inflammation in cell models using hyperpolarized ^{13}C-pyruvate. *Theranostics*. 2018;8:3400-3407.
61. Rosenfeld D, Zur Y. Design of adiabatic selective pulses using optimal control theory. *Magn Reson Med*. 1996;36:401-409.
62. Skinner TE, Reiss TO, Luy B, Khaneja N, Glaser SJ. Application of optimal control theory to the design of broadband excitation pulses for high-resolution NMR. *J Magn Reson*. 2003;163:8-15.
63. Waldman A, Rees JH, Brock CS, Robson MD, Gatehouse PD, Bydder GM. MRI of the brain with ultra-short echo-time pulse sequences. *Neuroradiology*. 2003;45:887-892.
64. Larson PEZ, Han M, Krug R, et al. Ultrashort echo time and zero echo time MRI at 7T. *MAGMA*. 2016;29:359-370.
65. Johnson KM, Fain SB, Schiebler ML, Nagle S. Optimized 3D ultrashort echo time pulmonary MRI. *Magn Reson Med*. 2013;70:1241-1250.

How to cite this article: Somai V, Kreis F, Gaunt A, et al. Genetic algorithm-based optimization of pulse sequences. *Magn Reson Med*. 2021;00:1–15. doi:10.1002/mrm.29110